Inhibition of the second phase precipitation and improvement of intergranular corrosion resistance by boron segregation at the grain boundary of S31254 superaustenitic stainless steel

Wang, Jian; Liu, Zhiqiang; Tian, Haiyu; Han, Peide; Gonzalez-Garcia, Yaiza

DOI
10.1016/j.corcom.2023.08.006

Publication date
2024

Document Version
Final published version

Published in
Corrosion Communications

Corrosion Communications 15 (2024) 1–12

Contents lists available at ScienceDirect

Corrosion Communications

journal homepage: www.elsevier.com/locate/corcom

Research Article

Inhibition of the second phase precipitation and improvement of intergranular corrosion resistance by boron segregation at the grain boundary of S31254 superaustenitic stainless steel

Jian Wang [a,*], Zhiqiang Liu [a], Haiyu Tian [a], Peide Han [a,*], Yaiza Gonzalez-Garcia [b]

[a] College of Materials Science and Engineering, Taiyuan University of Technology, Taiyuan 030024, China
[b] Delft University of Technology, Department of Materials Science and Engineering, Mekelweg 2, 2628 CD, Delft, the Netherlands

ARTICLE INFO

Article history:
Received 30 June 2023
Received in revised form 15 August 2023
Accepted 15 August 2023
Available online 1 April 2024

Keywords:
Superaustenitic stainless steel
S31254
Boron
Sigma phase
Corrosion

ABSTRACT

The inhibition of Mo segregation and phase precipitation is vital for improving the hot workability and corrosion resistance of superaustentic stainless steels (SASS). The boron non-equilibrium segregation of S31254 SASS was implemented through solid solution, air cooling, and diffusion at low-temperature treatment (SADT). The precipitation process and intergranular corrosion (IGC) of S31254 SASS with various boron distributions were researched at a sensitive temperature. The second phases were observed and identified by SEM and TEM. IGC susceptibility was evaluated by double-loop potentiodynamic reactivation (DL-EPR) measurements. The SADT treatment promoted more segregation of B at the grain boundary, leading to lower amounts of grain boundary precipitation before aging for 6 h. The decrease of σ phases in B-regulated samples enhances the IGC resistance, compared with the samples without B addition specimens.

1. Introduction

S31254 super-austenitic stainless steel (SASS), a kind of high alloy stainless steel with high content of Cr, Ni, and Mo, has exhibited excellent mechanical properties and corrosion resistance comparable to nickel-based alloys. SASS is widely used in petrochemical, papermaking, seawater desalination, and other very harsh corrosion environments [1–3]. However, the increase in element addition amounts such as Mo and Cr leads to the formation of brittle second phases during solidification, hot-deformation, or heat-treatment processes, which seriously deteriorate the mechanical and corrosion properties of the alloys [4–7]. Therefore, it is vital to control the Mo segregation and the second phase precipitation to improve the hot ductility and obtain high-performance super-austenitic stainless steel [8–11].

The most common precipitates in SASS are sigma (σ), Chi (χ), Laves, and Cr_2N phase. Several investigations have found that the metastable Laves phase is first formed and then transformed into σ phase, when 6Mo SASS is aged in the temperature range of 650–950 °C [12–14]. The phase formation is closely related to the diffusion of elements, so it is expected to regulate the precipitation distribution by adding some appropriate beneficial elements and controlling the segregation of elements at the grain boundaries. Previous studies have found that Cr and Mo have a great driving force for the formation of σ phase [15]. The 0.25 % Nb and 2.2 % Mn were discovered to stabilize the alloy and improve the mechanical properties of S31254 steels [16]. The addition of W to 7Mo SASS delayed the phase transition process from χ or Laves phases to σ phase, thus indirectly controlling the precipitation of σ phase [17]. The introduction of suitable Co into 7Mo SASS also inhibited the formation of σ phase to a certain extent [18]. Appropriate Ce addition to SASS can also be utilized to promote ferrite (δ) nucleation in interdendritic, and Mo segregation and σ-phase precipitation were controlled to a certain extent [19,20].

Compared with other elements, boron is insoluble in austenite and tends to segregate to grain boundaries [21–23]. Yao demonstrated that non-equilibrium boron segregation enhances the grain boundary hardening of 304 austenitic stainless steel containing 33 mg/L boron [24].

* Corresponding authors.
E-mail addresses: wangjian@tyut.edu.cn (J. Wang), hanpeide@tyut.edu.cn (P. Han).

https://doi.org/10.1016/j.corcom.2023.08.006

The $(Cr, Fe)_{23}(C, B)_6$ carbides and $(Cr, Fe)_2B$ borides were formed along the boundary after aging treatment from 750 ˚C to 1050 ˚C. Other investigations also observed boron segregation at the grain boundaries of AISI 316 L steel. Fe-, Cr-, and Mo-rich precipitates, including M_2B, M_5B_3, and M_3B_2, were detected in the steel specimens with high B content (40 mg/L) [25,26]. In addition, boron was detected in the austenite grain boundaries of heat-resistant steels during austenitization. In this case, $M_{23}C_6$ carbides partitioned to form $M_{23}(C, B)_6$ [27,28].

For the super-austenitic steels, the formation of σ phases can also be inhibited by adding B to the alloy during manufacturing or subsequent heat treatment. Several studies have demonstrated that the chromium-depleted region near the grain boundary of B-added S31254 SASS decrease, leading to the enhancement of corrosion resistance [29–32]. Recently, the segregation of B at the grain boundary of S32654 steels was also detected by 3D ATP, and the hot-deformation was greatly improved due to the decrease of second phases in B-added S32654 steels [33]. Further, the dissolution and segregation of boron in austenitic stainless steels depend on the heat treatment time and temperature. The maximum solubility of boron was found to be 97 mg/L at 1125 ˚C in 18 %Cr-15 %Ni steel. As the temperature decreases, the solubility decreases to less than 30 mg/L at 900 ˚C [34]. Especially, non-equilibrium boron segregation occurs when the steel cools from a high solution treatment temperature [35,36]. Recently, the solid solution, air cooling, and diffusion at low-temperature treatment (SADT) were implemented in S31254 steels that contain B and Ce, and the grain boundary co-segregation of B and Ce hinders the precipitation of second phases and improves the mechanical properties [37].

This work implements the 40 mg/LB-added S31254 through the SADT treatment to promote boron non-equilibrium segregation near grain boundaries. The susceptibility to intergranular corrosion (IGC) and the influence of precipitates at the grain boundary were studied. This paper aims to regulate boron segregation at the grain boundary and clarify its effect on the phase precipitation process. This investigation may contribute to a meaningful understanding of the boron segregation behavior in S31254 SASS and provide a favorable technology for controlling the phase precipitation of superaustenitic stainless steels.

2. Experimental

2.1. Preparation for experimental materials

The chemical composition of SASS specimens is shown in Table 1. S31254 ingots without B and with 40 mg/L B (named 0B and 40B, respectively) were prepared by a vacuum induction furnace. The ingot was subsequently homogenized at 1250 ˚C for 12 h and hot rolled into a 12 mm thick plate. After that, the plate was cut into 15 mm × 15 mm × 3 mm square blocks by a wire-cutting machine. The B non-equilibrium segregation is determined by the following two methods: (i) step solid-solution method and (ii) SADT treatment. In the case of step solid-solution, the two hot-rolled S31254 samples without and with B-addition are subjected to heat at 1180 ˚C for 30 min and cooling to 1100 ˚C at a rate of 4 ˚C/min with an insulating time for 15 min, and then quickly quenching at the water. These specimens are called 0B-SS and 40B-SS. In the SADT treatment, the B-added sample was kept at 1180 ˚C for 30 min, then cooled to 1100 ˚C in the furnace within 15 min, and final air-cooling. Subsequently, the air-cooled samples were further held at 300 ˚C low-temperature treatment for 20 min and then quenched in water. This SADT treated specimen is called 40B-300 [37]. Finally, the 0B-SS, 40B-SS, and 40B-300 samples were further sensitized at 950 ˚C for 30 min, 2 h, and 6 h, respectively.

2.2. Microstructure characterization

All samples were ground with SiC papers step by step to 2500 grit, polished like a mirror, cleaned with ethanol and distilled water in an ultrasonic bath, and etched with aqua regia for observation. The microstructure was characterized by Leica, DM 6 M optical microscope (OM), EVO18 scanning electron microscope (SEM), and the energy dispersive spectrometer (EDS, SHIMADZU electron probe micro-analyzer) was used to determine the elemental content and distributions. The number and size of precipitates were counted by Image-Pro Plus (IPP) software. A JEOL 2100F field emission transmission electron microscope (TEM) with a super-X energy-dispersive X-ray spectroscopy (EDS) system is further employed to analyze the microstructure. The specific TEM foils were prepared by a focused ion beam (FIB) milling technique. To predict the mass fraction of boron dissolved in the alloy with temperature, a thermodynamic calculation was done using ThermoCalc software.

The scanning Kelvin probe force microscopy (SKPFM) measurements were performed in tapping mode using a Bruker Dimension Edge™ instrument with Nanodrive v8.05 software. A rectangular conductive cantilever (silicon pyramid single-crystal tip coated with PtIr5, SCM-Pit probe) was employed. A direct current (DC) bias potential was applied to the AFM tip for all measurements. The scanned area was 20 μm^2 with a scan rate of 0.5 Hz and a pixel resolution of 512 × 512. All measurements were performed on freshly polished samples at room temperature.

2.3. Electrochemical measurements

The electrochemical measurements were carried out in a typical three-electrode system on a CS350 electrochemical workstation at room

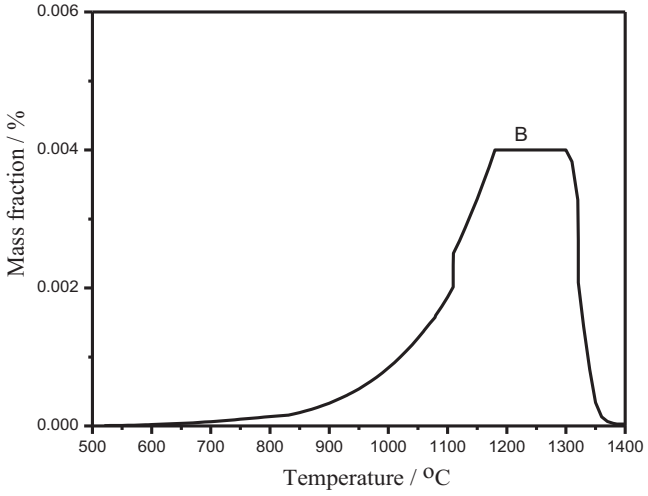

Fig. 1. Solubility curve of B for the 40B steel as a function of the temperature.

Table 1
Chemical composition of 0B and 40B steels (mass fraction, %).

Sample	C	Si	Mn	P	S	Cr	Ni	Mo	Cu	N	B	Fe
0B	0.010	0.61	0.43	0.024	0.001	20.18	18.00	6.00	0.69	0.193	–	Bal.
40B	0.014	0.62	0.94	0.014	0.003	20.15	18.11	6.12	0.72	0.20	0.004	Bal.

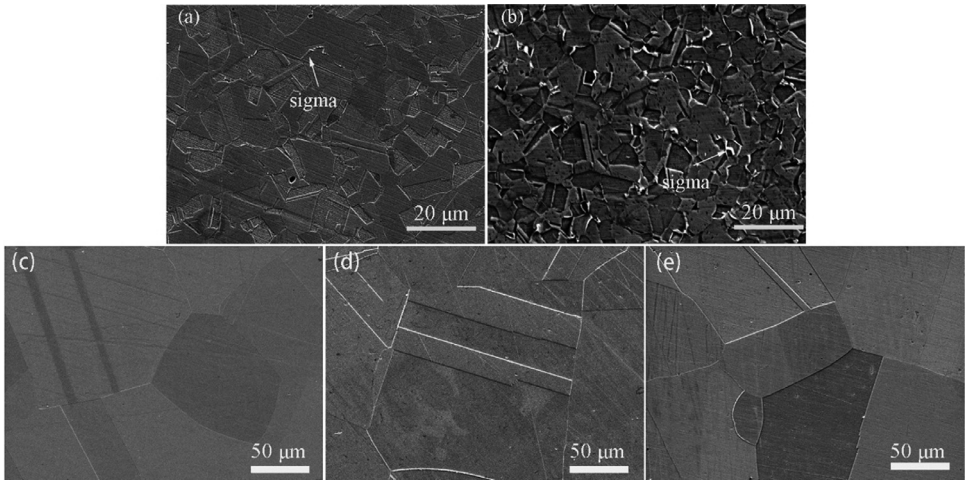

Fig. 2. SEM images of the hot-rolled (a) 0B and (b) 40B alloys, and the (c) 0B-SS, (d) 40B-SS and (e) 40B-300 steels.

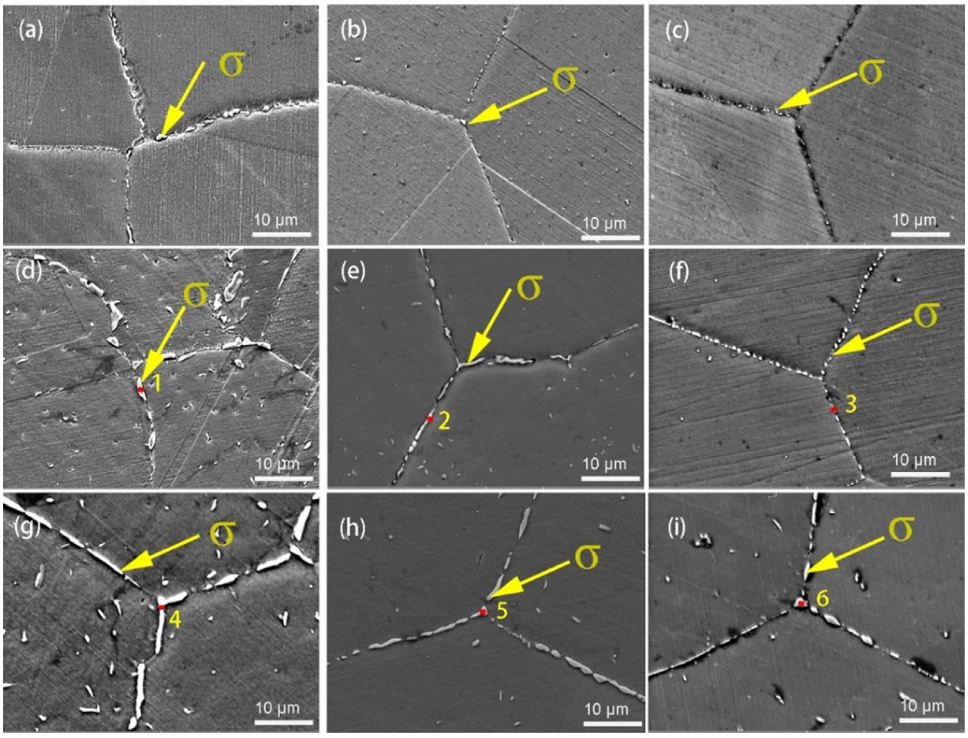

Fig. 3. SEM images of (a, d, g) 0B-SS, (b, e, h) 40B-SS, and (c, f, i) 40B-300 steels after aging at 950 °C for (a-c) 30 min, (d-f) 2 h and (g-i) 6 h.

temperature. The specimens with an exposed area of 1 cm × 1 cm, a platinum foil, and a saturated calomel (SCE) were used as the working, counter, and reference electrodes, respectively. The DL-EPR measurements were carried out in a mixed solution of 0.01 mol/L KSCN, 2 mol/L H_2SO_4, and 2 mol/L HCl at room temperature. The polarization range was applied from open circuit potential (OCP) to 200 mV, held for 2 min, and cathodically polarized back to the OCP potential value. The scanning rate was 1.667 mV/s [29]. The reactivation peak current (I_R) and activation peak current (I_a) were recorded for the calculation of the degree of sensitization (DOS/% = 100 × I_r/I_a). All experimental experiments were replicated three times for reproducibility.

3. Results and discussion

3.1. Microstructure of heat-treated 0B and 40B steels after boron segregation

Since B tends to segregate towards the grain boundary, the curve of B solubility in 40B steels as a function of temperature was calculated using ThermoCalc software (shown in Fig. 1). The B with the maximum solubility of 0.004 wt.% dissolves into austenite at about 1200–1300 °C, while only part of the B dissolves into the austenite matrix in the range of 1080–1180 °C. Generally, non-equilibrium segregation that occurs at the cooling stages is correlated with the temperature and cooling rate.

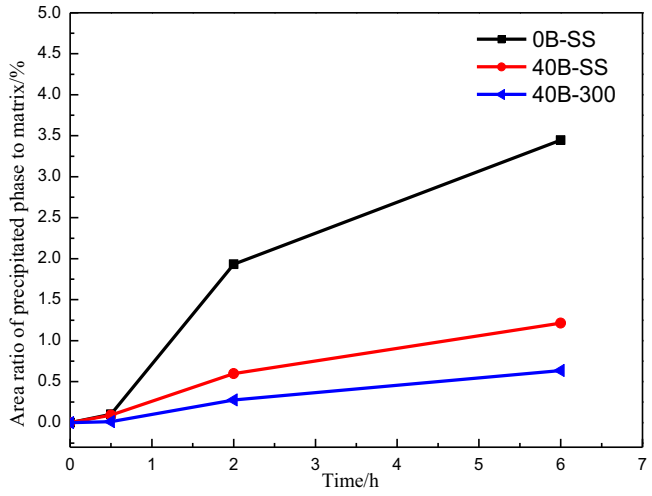

Fig.4. Precipitates-matrix ratio evolution as a function of aging exposure time.

Therefore, a step solid solution process for 40B steel is proposed, consisting of heating the specimen at 1180 °C for a period of time and then slowly cooling it to 1100 °C for thermal insulation. The purpose is to release a portion of B (about 0.002 wt.%) into the grain boundary based on the non-equilibrium segregation. Further, B will be completely insoluble in the matrix below 700 °C, so the SADT treatment conducted on the 40B samples is expected to maximize the non-equilibrium segregation of B into the grain boundary. The segregation of B at grain boundaries with different concentrations would play a vital role in the precipitation of the second phase.

The SEM images of hot-rolled 0B and 40B steels are shown in Fig. 2(a, b). Both types of samples have smaller grains, and a few secondary phases are observed in each sample. Further SEM analysis allowed us to confirm the influence of step solid-solution treatment and low-temperature holding on the microstructure. As shown in Fig. 2(c, d), the grain size of the hot-rolled 0B and 40B steels after step solid-solution treatment is larger, but the precipitates were completely dissolved into the matrix of 0B-SS and 40B-SS alloys. After further SADT treatment, the grain size of 40B-300 steel detected in Fig. 2(e) showed little change in comparison to step solid-annealed samples, and no second phases were observed, indicating that the SADT treatment only affects the segregation of elements and has no significant influence on the microstructure.

High-resolution SEM images confirmed the precipitation changes of different samples (shown in Fig. 3(a, b)). The secondary phases were preferentially precipitated at the grain boundaries when 0B-SS and 40B-SS samples were aged at 950 °C for 30 min. Fig. 3(d) displays that the precipitated phase at the grain boundary of 0B-SS is significantly coarsened after aging for 2 h, while the grain boundary phases at 40B-SS shown in Fig. 3(e) are still intermittently distributed. It is also noted from Fig. 3(g, h) that the aged-6 h 0B-SS samples contain more precipitates in the matrix than those of 40B-SS, indicating that partial B segregation of 40B-SS at the grain boundary slows down the precipitation of the second phase. The precipitates of 40B-300 samples presented in Fig. 3(c, f, i) are discontinuously distributed at the grain boundary and less than that of 40B-SS before aging for 6 h, which shows that SADT treatment is indeed conducive to the segregation of more boron at the grain boundary. Especially, the amount of phases in aged-0.5 h and aged-2 h 40B-300 alloys is lower at the grain boundary and in the matrix compared to 40B-SS samples. This is further explained in the discussion.

The volume fraction of the precipitated phases was calculated, and the evolution of precipitate-matrix area ratio as a function of aging exposure time is presented in Fig. 4. It can be seen that the precipitation rate of the second phase before the 6 h aging stage is: 40B-300 < 40BSS < 0BSS. The element contents in grain boundary precipitates located in positions 1–9 of different aging times are presented in Table 2. The majority of precipitates have Mo and Cr contents of about 20 wt.% [17,38], so the grain boundary precipitates can be assigned to σ phases.

To confirm the element distribution of the specimens after aging treatment, element mapping was carried out for the samples aged for 2 h (Fig. 5). It was found that Mo tends to segregate towards the grain boundary in all samples, but no enrichment of other elements was detected. This suggests that Mo-rich σ phases are mainly precipitated.

The element mapping of the 0B-SS, 40B-SS, and 40B-300 samples aged for 6 h are shown in Fig. 6, respectively. For the 0B-SS steels, Mo

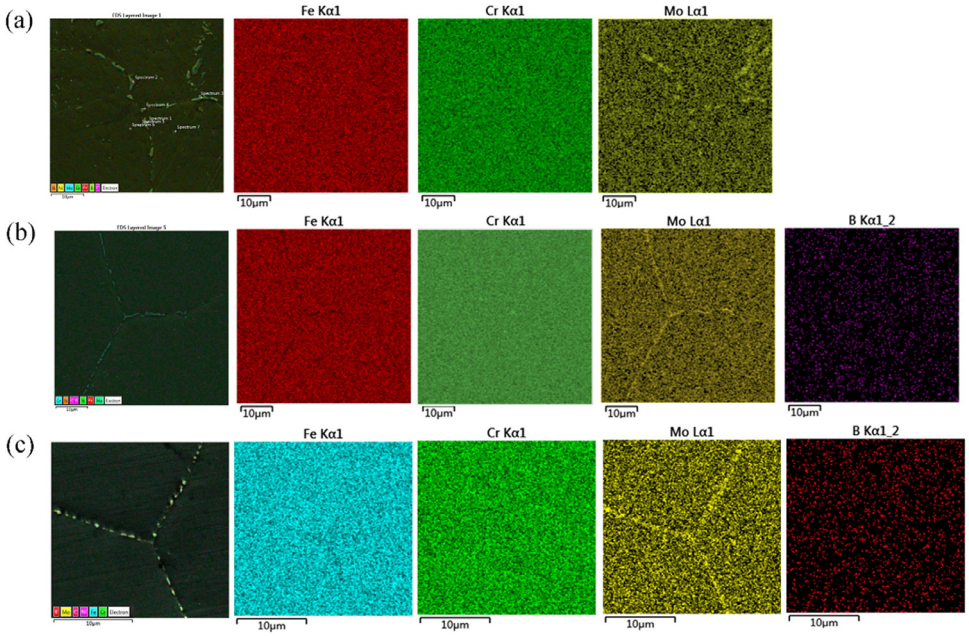

Fig. 5. Elemental distributions by mapping of (a) 0B-SS, (b) 40B-SS, and (c) 40B-300 alloy aged for 2 h.

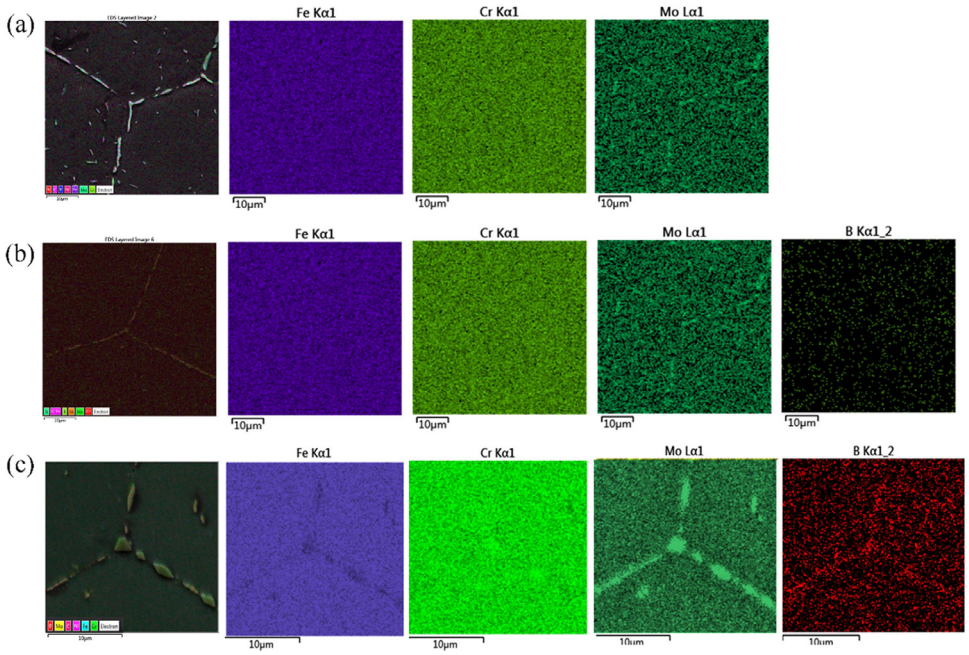

Fig. 6. Elemental distributions mapped of (a) 0B-SS, (b) 40B-SS, and (c) 40B-300 alloy aged for 6 h.

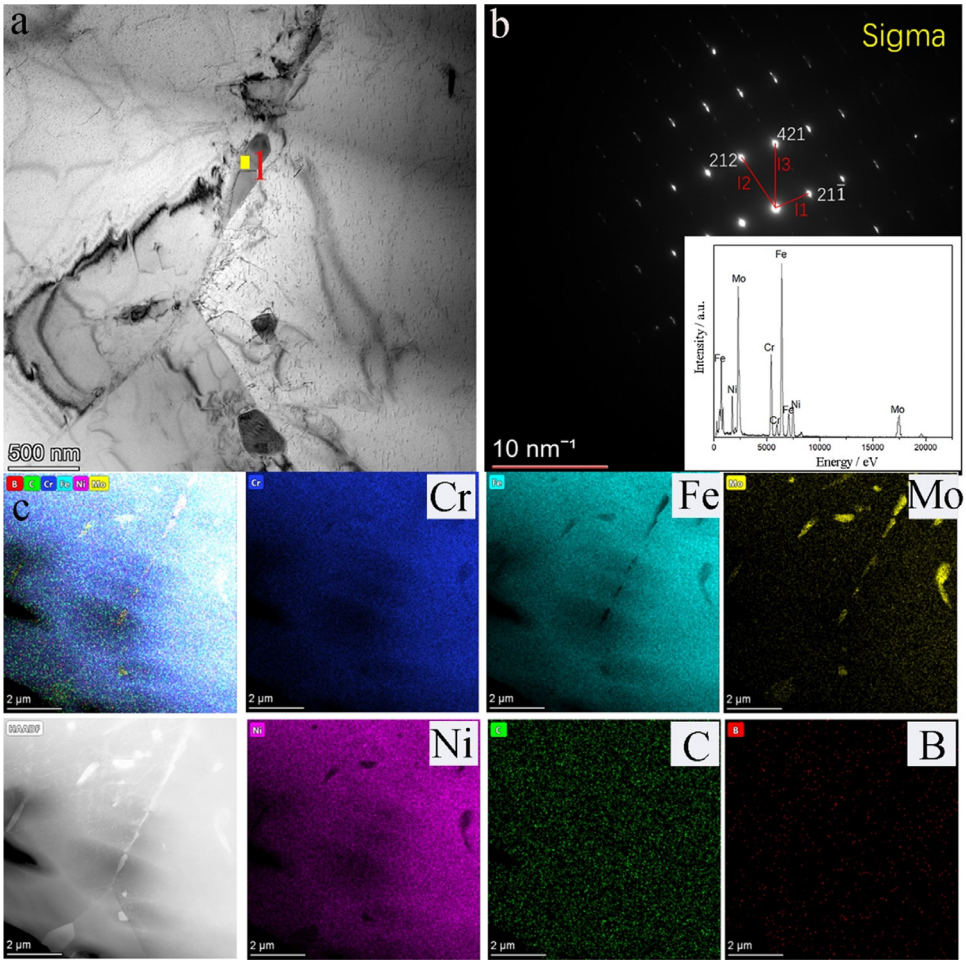

Fig. 7. (a) TEM and (b) SAED maps and (c) corresponding STEM-EDS elemental composition of grain boundary precipitates in 0B-SS alloy aged for 6 h.

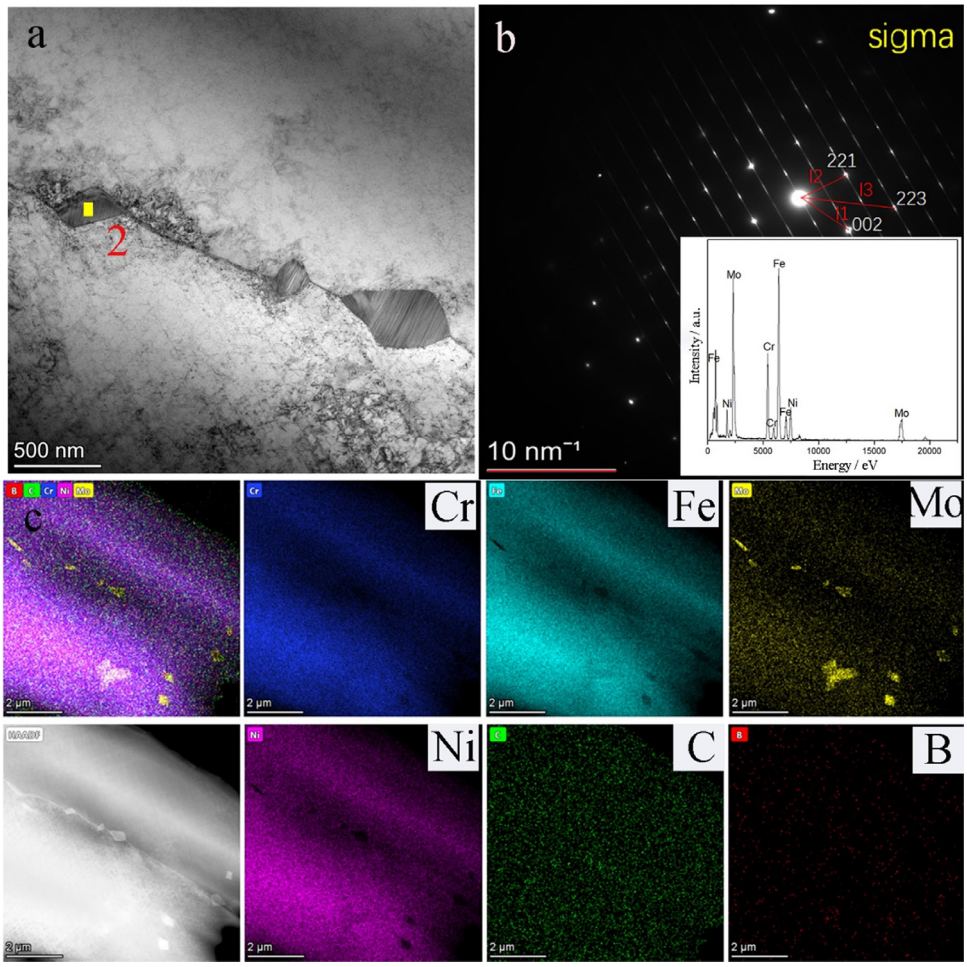

Fig. 8. (a) TEM and (b) SAED maps and (c) corresponding STEM-EDS elemental composition of grain boundary precipitates in 40B-SS alloy aged for 6 h.

Table 2
Main compositions (mass fraction / %) of the selected precipitates in grain boundary precipitates in Fig. 3(d-i) by SEM/EDS analysis.

Point	Fe	Cr	Ni	Mo
No. 1	40.91	21.77	9.08	21.14
No. 2	37.44	24.04	13.67	16.37
No. 3	42.16	22.14	10.46	17.48
No.4	41.51	22.39	7.81	21.86
No.5	42.75	22.96	8.65	20.92
No. 6	45.74	23.61	9.79	17.14

Table 3
Main compositions (mass fraction / %) of the selected precipitates in grain boundary precipitates in Figs. 7(a), 8(a) and 9(a) from TEM observation.

Point	Fe	Cr	Ni	Mo
No. 1	38.68	16.75	7.19	30.57
No. 2	39.74	17.62	7.77	31.93
No.3	46.18	30.48	8.67	11.73

segregates to the grain boundary, and Cr gradually enriches in the grain boundary. Moreover, B segregation was hardly detected in 6 h-aged 40B-SS samples, which may be due to the lower amount of B segregation. However, besides a large amount of Mo segregation, B can be clearly observed in the grain boundary region of 40B-300 samples, indicating that a higher content of B exists in the precipitates and grain boundary.

Figs. 7-9 show the TEM analysis of the 0B-SS, 40B-SS, and 40B-300 specimens aged at 950 °C for 6 h, respectively. It can be observed that some phases at grain boundaries were found in all samples, and the corresponding EDS results of the precipitates in various specimens are given in Table 3. As for the 0B-SS and 40B-SS samples, the SAED and EDS shown in Figs. 7(b), 8(b), and 9(b) identified that the precipitates at the grain boundary are σ-phase with a higher Mo and Cr content, and the STEM-EDS maps of Figs. 7(c) and 8(c) display that Mo has a significant segregation trend toward grain boundaries. However, the STEM-EDS maps of several elements display B segregating to the grain boundaries in 40B-steels aged for 6 h (Fig. 9(c)), which is similar to the EPMA observation shown in Fig. 6(c). The co-segregation of B and Mo at the grain boundaries further provides evidence that B and Mo are the constituent elements of grain-boundary phases.

3.2. Intergranular corrosion of 0B and 40B steels treated with B redistribution after aging at 950 °C

The IGC of 0B-SS, 40B-SS, and 40B-300 samples were evaluated using the DL-EPR method. The DL-EPR curves with typical I_a and I_r are shown in Fig. 10. In the anodic scan, the current is increased after the activation of the whole sample surface. The reactivation current peak

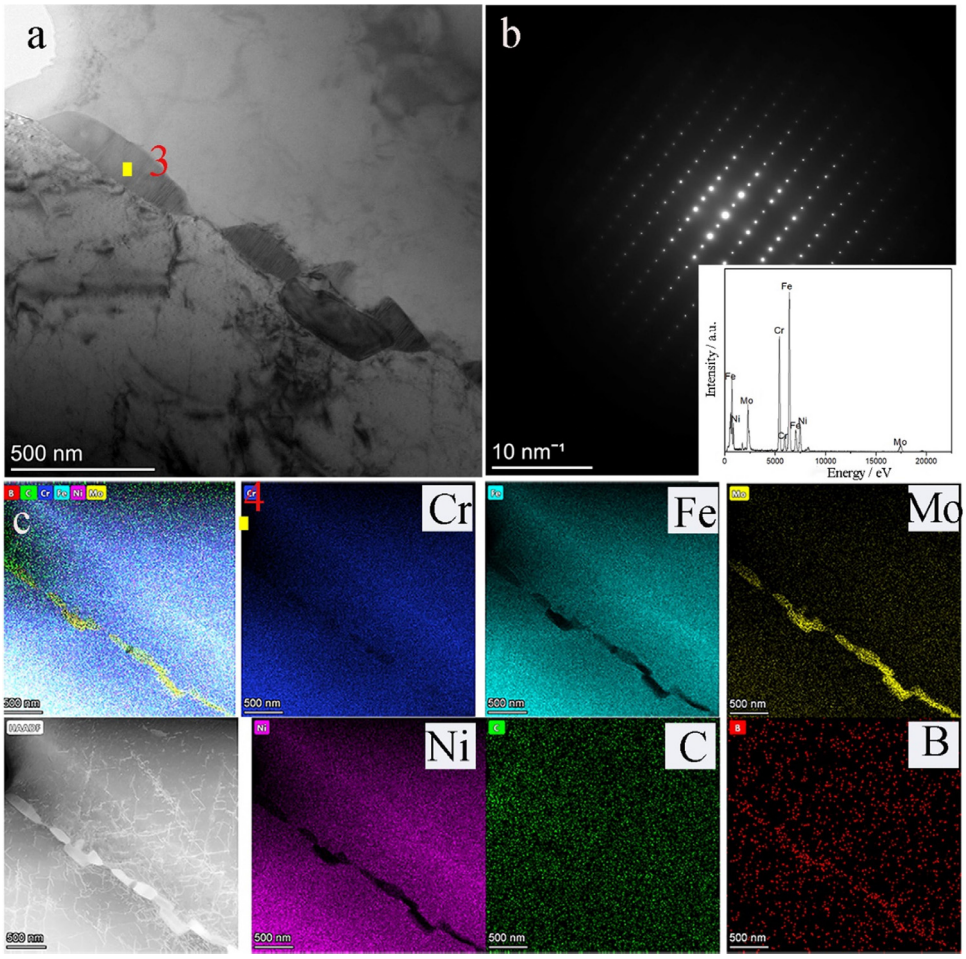

Fig. 9. (a) TEM and (b) SAED maps and (c) corresponding STEM-EDS elemental composition of grain boundary precipitates in 40B-300 alloy aged for 6 h.

is mainly derived from the Cr- and Mo-depleted regions. Moreover, due to the Ohmic resistance drop, the potentials corresponding to I_a and I_r are not consistent, which can also be found in previous works [39–41]. The DOS value can be used to quantify the degree of sensitization of different samples [42,43]. As shown in Fig. 11, the DOS values of all the specimens gradually increase with aging time, suggesting that the susceptibility to IGC increases. Before aging for 6 h, the DOS values at the same aging time are related to the amount of precipitates presented at their grain boundaries, following this ranking 40B-300 < 40B-SS < 0B-SS. This indicates that boron segregation and precipitation regulation at the grain boundary are beneficial to improving the steel's resistance against IGC.

Fig. 12 displays the surface micrographs of 0B-SS, 40B-SS, and 40B-300 specimens aged at 950 ˚C for various exposure time after the DL-EPR measurements. The IGC attack for all the samples becomes more severe and wider at the grain boundaries with the increase in aging time. This can be attributed to the much more serious Cr- and Mo-depleted zone generated from the growth and coarsening of the precipitates [44]. However, the IGC attacks at the 40B-300 specimens seem lower than 40B-SS or even lower than 0B-SS before aging for 6 h, indicating that there are fewer precipitates distributed at the grain boundary.

Fig. 13 shows the topography and surface voltaic potential maps of different samples by SKPFM measurement. The potential differences indicate the different reactivity of the surface. It is observed that there are large differences in the grain boundaries. As displayed in Fig. 13(b, d, e), the phase precipitates cause the discontinuity of the passivation film at the grain boundary, and the chromium and molybdenum depleted zones appear, so the difference of volta potential between the intragranular area and grain boundary can be observed. However, the 40B-300 sample has the lowest grain boundary potential values. The differences are narrowly located between the grain boundary and the intragranular area, resulting in a lower degree of intergranular corrosion. In previous research, the large potential difference between oxide surface and inclusions of 316 L austenitic stainless steel [45] and grain boundary and grain in aged 904 L steel [46] was also associated with high intergranular corrosion susceptibility, which is similar to the results obtained in this work.

3.3. Mechanism on the inhibition of second phase precipitation and improvement of intergranular corrosion resistance by boron non-equilibrium segregation

The 40B-SS exhibited a much less precipitate amount of grain-boundary phase than the 0B-SS specimens. It has been reported that adding B to Ni-base alloys can control and retard the precipitation of the second phases. For instance, the precipitation time and temperature of $M_{23}C_6$ in Nimonic 105 superalloys shifted higher after boron addition [47]. Due to the inhibition of Ti diffusion toward the grain boundary, the 0.002 wt.% B addition greatly reduces the phase precipitation in 30Ni-15Cr-1.3Mo-2.4Ti-0.3Al-0.25Si-Fe alloys [48]. The super-austenitic has a similar structure to Ni-base alloys, and it can be speculated that there are two reasons why boron hinders the nucleation and growth of the σ phase. On the one hand, with the gradual increase of B content at the grain boundary, most of the positions at the grain boundary are occu-

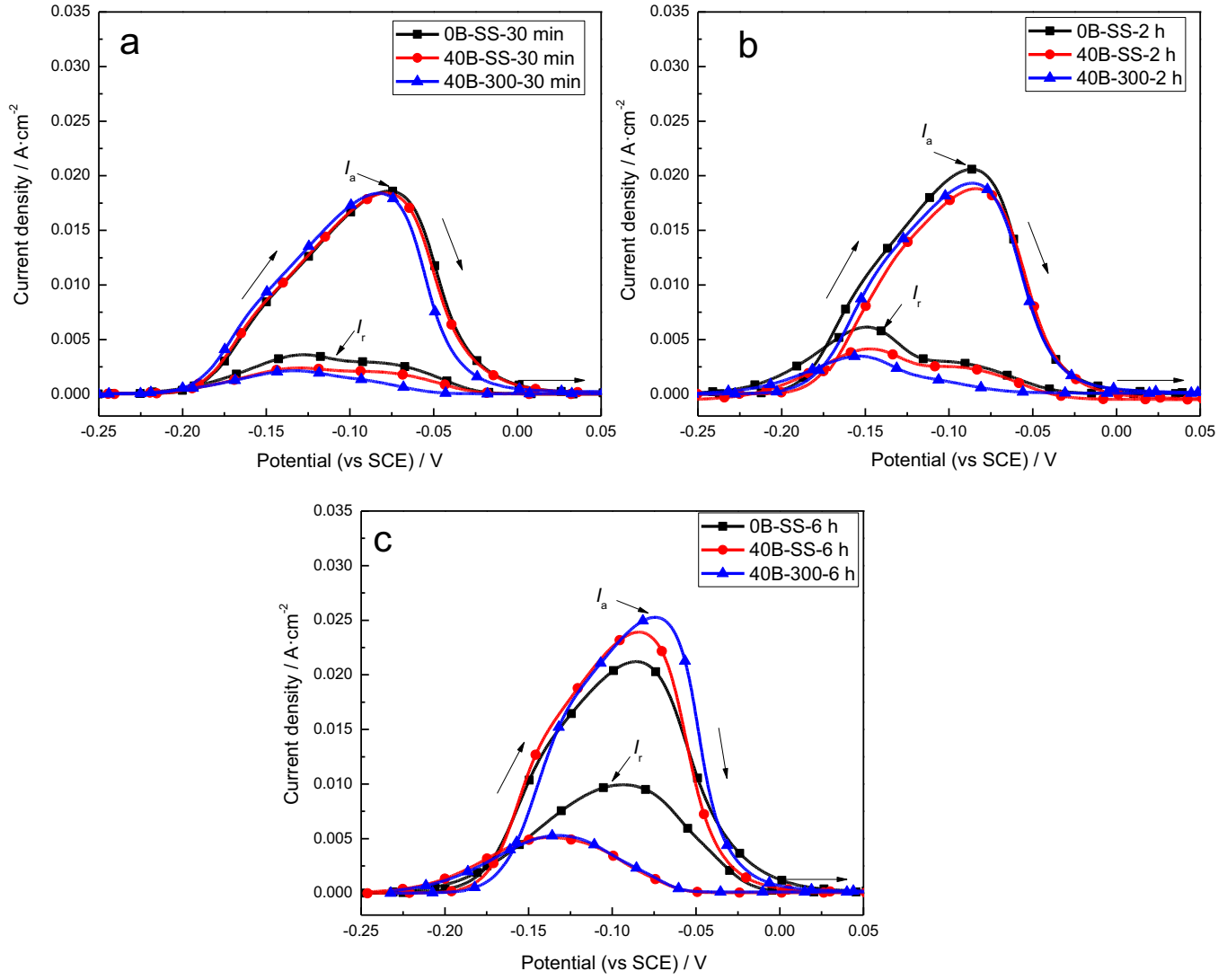

Fig. 10. DL-EPR curves of 0B-SS, 40B-SS, and 40B-300 samples aged at 950 °C for (a) 30 min, (b) 2 h and (c) 6 h.

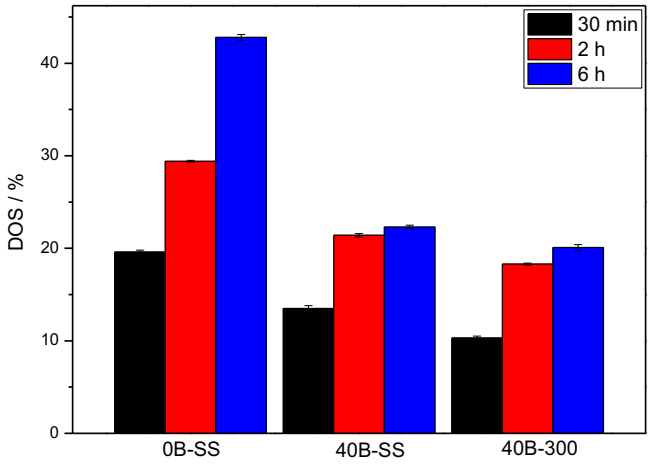

Fig. 11. DOS comparison of 0B-SS, 40B-SS and 40B-300 aged for different aging time.

pied by B, which will reduce the nucleation rate of the σ phase during aging. On the other hand, boron segregation to the grain boundary improves the cohesive strength of grain boundaries, which will reduce the diffusion rate of Mo and Cr forming σ-phase along the grain boundary, thus inhibiting the growth process of σ-phase in the alloy. In previous work, the S31254 with boron addition also exhibited a well-inhibitory effect of σ-phase precipitation along grain boundaries [29], and the suppression of Mo diffusion after B addition in the S31254 SASS was also proved based on the first principle calculation [49].

Therefore, we propose the following mechanism, shown in Fig. 14, to explain the inhibition of second-phase precipitation and improvement of intergranular corrosion resistance by boron non-equilibrium segregation. The step solid-solution treatment caused the non-equilibrium segregation of partial B on the boundary of 40B-SS, so the Mo diffusion and the σ-phase precipitation at the grain boundary were inhibited in the initial aging period. However, some B atoms at the grain boundary are also easily diffused toward the intracrystalline defect site, prolonging the aging time and resulting in a gradual decrease in grain boundary inhibition of phase precipitation after aging for 6 h (Fig. 3(g, h)). After the low-temperature holding treatment process, B in the 40B-300 alloys is fully segregated to the grain boundary, and the segregation of Mo and Cr from the matrix to the grain boundary is suppressed, which causes the

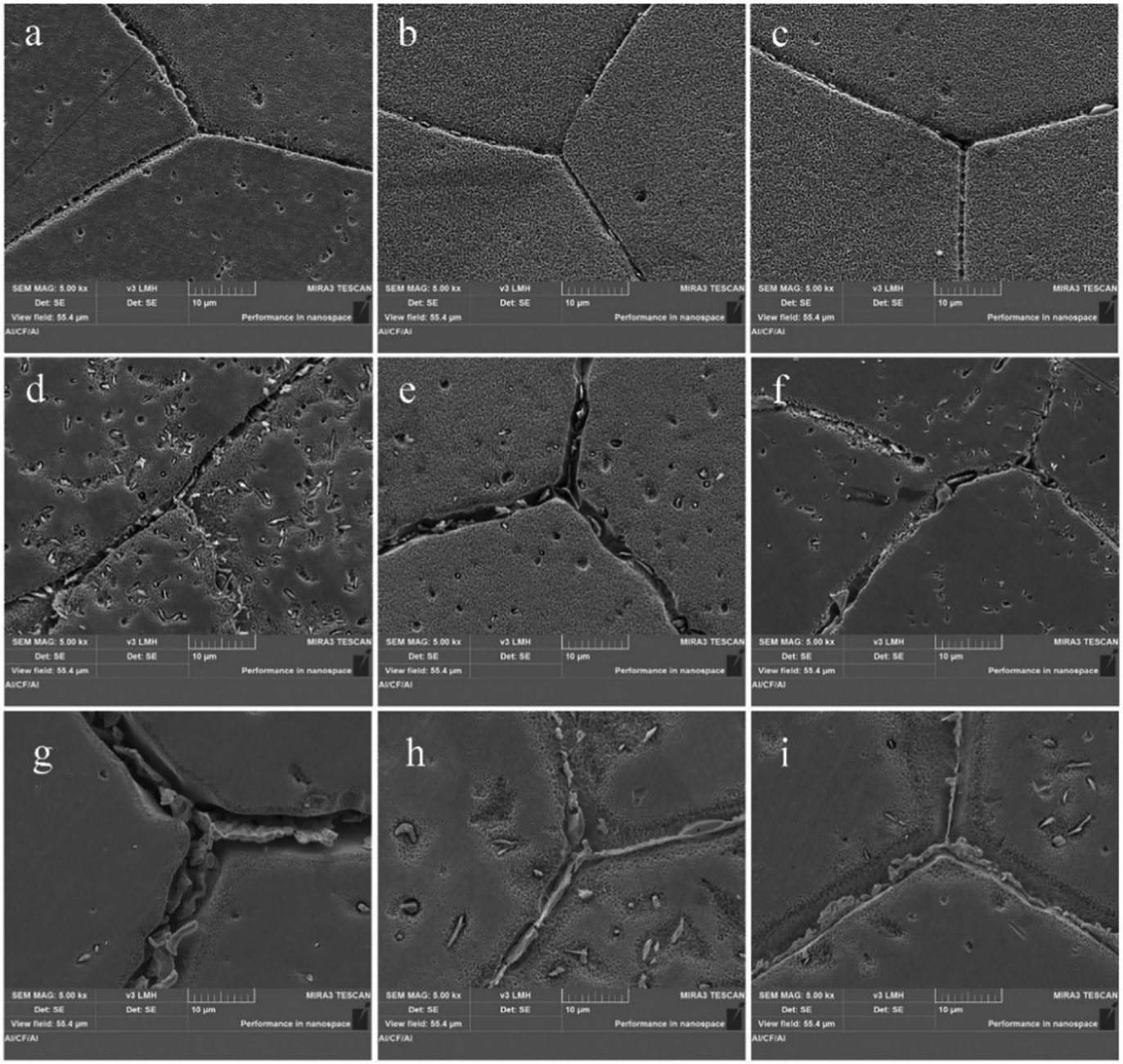

Fig. 12. SEM images of intergranular attack after DL-EPR experiments on (a, d, g) 0B-SS, (b, e, h) 40B-SS and (c, f, i) 40B-300 specimens after aged at 950 °C for (a-c) 30 min, (d-f) 2 h and (g-i) 6 h.

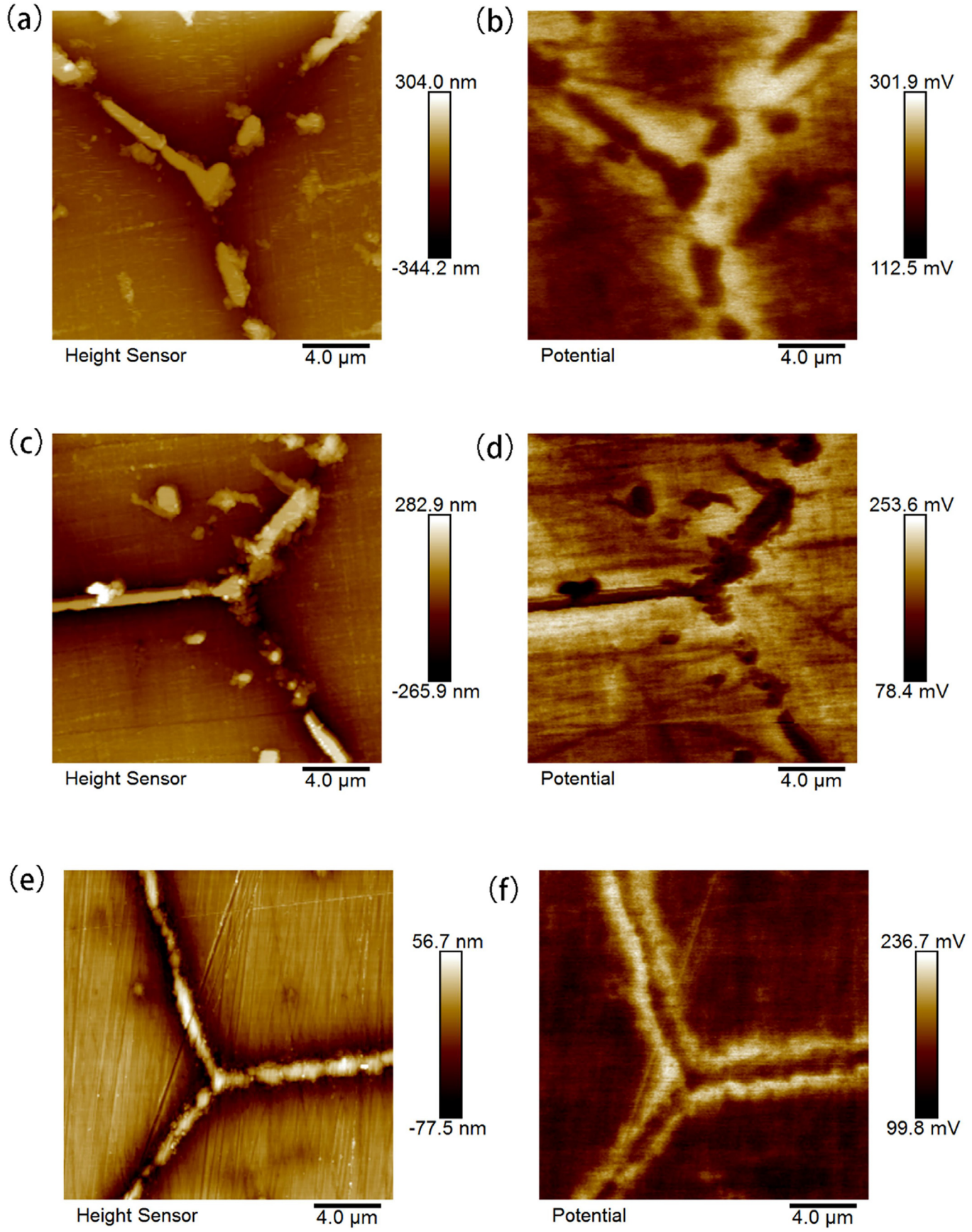

Fig. 13. (a, c, e) AFM topography and (b, d, f) volta potential (SKPFM) maps of (a, b) 0B-SS, (c, d) 40B-SS, and (e, f) 40B-300 samples.

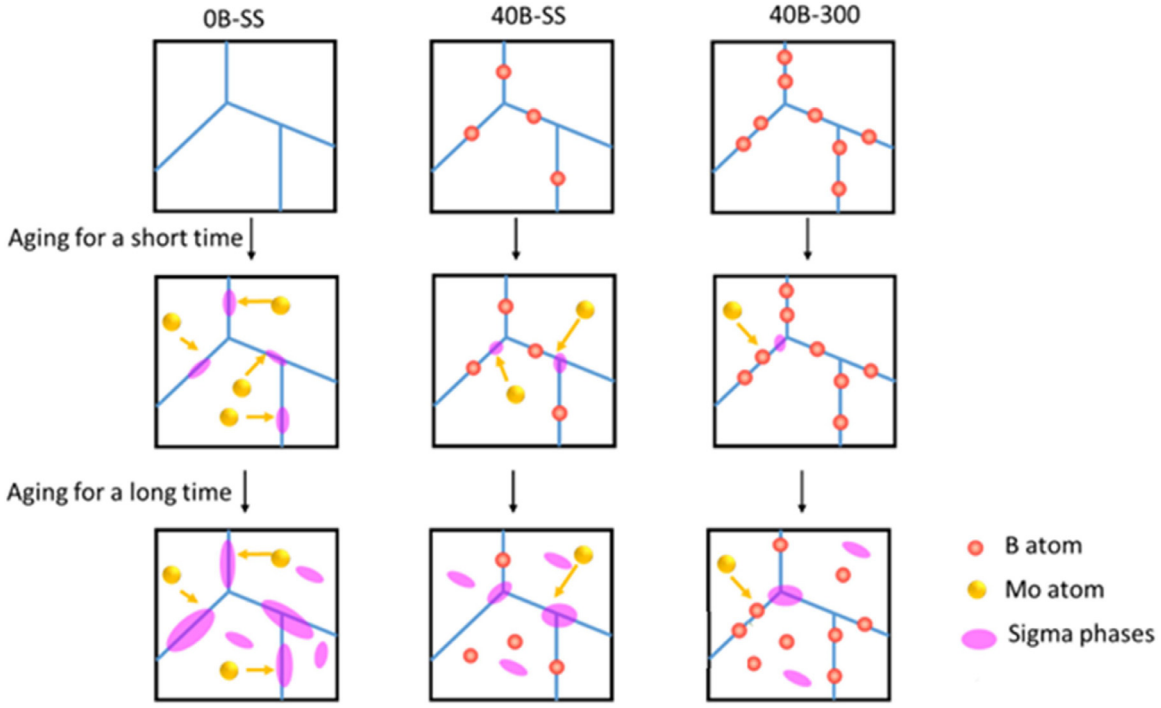

Fig. 14. Schematic diagram of the inhibition mechanism inhibition of second-phase precipitation and improvement of intergranular corrosion resistance by boron non-equilibrium segregation. The precipitates change through boron regulation in 6Mo stainless steels.

lower content of Mo and Cr distributed near the grain boundary, thus forming a few σ-phases. In addition, a notable phenomenon of Mo and B segregation at the grain boundary was seen in the aged-6 h 40B-300 samples, shown in Figs. 6(c) and 9(c). In addition, some B atoms are also pressable to segregate to the intracrystalline defects after a long-time aging treatment, which is also beneficial to the reduction of phase precipitation, so the phase numbers of 40B-300 are less than those of 40B-SS. Due to the regulation of grain boundary precipitation numbers, the IGC has been greatly enhanced in the 40B-300 specimens, due to the lower potential difference between intragranular and grain boundaries.

4. Conclusions

The boron segregation at the grain boundary of S31254 SASS is achieved by step-solid solution treatments and low-temperature heat preservation treatments based on non-equilibrium segregation. The precipitation process and intergranular corrosion (IGC) susceptibility of S31254 SASS with various boron distributions were improved after regulation of the B segregation. The main conclusions are shown as follows:

(1) A partial of B is biased to the grain boundary after step solid-solution treatment that was conducted on the 40 mg/L B-added S31254 subjected to heat at 1180 °C for 30 min and cool to 1100 °C at a rate of 4 °C/min with insulating time for 15 min, and then quickly quenching at the water. The combination of step solution and 300 °C low-temperature holing treatment promotes much more boron to segregate at the grain boundary.
(2) The grain boundary precipitates are lower for B-regulated specimens before aging for 6 h, especially for samples with step solid-solution and further low-temperature heat preservation, which the inhibition of σ-phase nucleation and Mo diffusion might explain.
(3) The coexistence of B and Mo along the grain boundary of B-regulated specimens can be observed with increased aging time.
(4) The decrease of σ-phases in B-regulated samples is beneficial to the enhancement of IGC resistance, compared with the samples without B addition specimens.

Declaration of competing interest

The authors declare that they have no known competing financial interests or personal relationships that could have appeared to influence the work reported in this paper.

Acknowledgments

This research was financially supported by the National Natural Science Foundation of China (52104338, U1860204 and 51871159) and China Scholarship Council (202006935035).

References

[1] T.T. Chen, J. Wang, Y. Zhang, P. Jiang, F.P. Yuan, P.D. Han, X.L. Wu, Twin density gradient induces enhanced yield strength-and-ductility synergy in a S31254 super austenitic stainless steel, Mater. Sci. Eng. A 837 (2022) 142727.
[2] K.T. Sunny, N.N. Korra, A systematic review about welding of super austenitic stainless steel, Mater. Today Proc. 47 (2021) 4378–4381.
[3] S.C. Zhang, H.B. Li, Z.H. Jiang, B.B. Zhang, Z.X. Li, J.X. Wu, H. Feng, H.C. Zhu, F. Duan, Chloride-and sulphate-induced hot corrosion mechanism of super austenitic stainless steel S31254 under dry gas environment, Corros. Sci. 163 (2020) 108295.
[4] R.W. Fonda, E.M. Lauridsen, W. Ludwig, P. Tafforeau, G. Spanos, Two-dimensional and three-dimensional analyses of sigma precipitates and porosity in a superaustenitic stainless steel, Metall. Mater. Trans. A 38 (2007) 2721–2726.
[5] R. Marin, H. Combeau, J. Zollinger, M. Dehmas, B. Rouat, A. Lamontagne, N. Loukachenko, L.L. Robert, σ-phase formation in super austenitic stainless steel during directional solidification and subsequent phase transformations, Metall. Mater. Trans. A 51 (2020) 3526–3534.
[6] G.W. Liu, Y. Han, Z.Q. Shi, J.P. Sun, D.N. Zou, Hot deformation and optimization of process parameters of an as-cast 6Mo superaustenitic stainless steel: a study with processing map, Mater. Des. 53 (2014) 662–672.
[7] E.X. Pu, W.J. Zheng, J.Z. Xiang, Z.G. Song, H. Feng, Y.L. Zhu, Hot working characteristic of superaustenitic stainless steel 254SMO, Acta Metall. Sin. 27 (2014) 313–323.
[8] L. Wang, Z.Y. Li, X. Hu, B. Lv, C. Chen, F.C. Zhang, Hot deformation behavior and 3D processing map of super austenitic stainless steel containing 7Mo–0.46 N–0.02 Ce: effect of the solidification direction orientation of columnar crystal to loading direction, J. Mater. Res. Technol. 13 (2021) 618–634.

[9] Y.S. Hao, J. Li, X. Li, W.C. Liu, G.M. Cao, C.G. Li, Z.Y. Liu, Influences of cooling rates on solidification and segregation characteristics of Fe-Cr-Ni-Mo-N super austenitic stainless steel, J. Mater. Proc. Technol. 275 (2020) 116326.
[10] Y.S. Hao, W.C. Liu, J. Li, B.X. Nie, W.N. Zhang, Z.Y. Liu, Microstructural bandings evolution behavior and their effects on microstructure and mechanical property of super-austenitic stainless steel, Mater. Sci. Eng. A 736 (2018) 258–268.
[11] C.C. Hsieh, W.T. Wu, Overview of intermetallic sigma (σ) phase precipitation in stainless steels, Int. Sch. Res. Not. 2012 (2012) 732471.
[12] T. Koutsoukis, A. Redjaïmia, G. Fourlaris, Phase transformations and mechanical properties in heat treated superaustenitic stainless steels, Mater. Sci. Eng. A 561 (2013) 477–485.
[13] Y.S. Hao, G.M. Cao, C.G. Li, J. Li, W.C. Liu, W.N. Zhang, Z.Y. Liu, The aging precipitation behavior of 20Cr-24Ni-6Mo super-austenitic stainless steel processed by conventional casting and twin-roll strip casting, Mater. Charact. 147 (2019) 21–30.
[14] J. Anburaj, S.S. Mohamed Nazirudeen, R. Narayanan, B. Anandavel, A. Chandrasekar, Ageing of forged superaustenitic stainless steel: precipitate phases and mechanical properties, Mater. Sci. Eng. A 535 (2012) 99–107.
[15] S.C. Zhang, H.B. Li, Z.H. Jiang, B.B. Zhang, Z. Li, J.X. Wu, S.P. Fan, H. Feng, H.C. Zhu, Effects of Cr and Mo on precipitation behavior and associated intergranular corrosion susceptibility of superaustenitic stainless steel S32654, Mater. Charact. 152 (2019) 141–150.
[16] J.P. Sanhueza, L.F. Montoya, E. Toledo, M.I. Alvarado, J. García, O. Prat, M.F. Meléndrez, D. Rojas, Design and characterization of super austenitic stainless steel stabilized with niobium produced by induction melting at open atmosphere, Steel Res. Int. 89 (2018) 1800215.
[17] S. Heino, Role of Mo and W during sensitization of superaustenitic stainless steel—crystallography and composition of precipitates, Metall. Mater. Trans. A 31 (2000) 1893–1905.
[18] L.H. Liao, J.Y. Li, Z.X. Zhao, F.H. Xu, W. Zhang, Precipitation and phase transformation behavior during high-temperature aging of a cobalt modified Fe-24Cr-(22-x)Ni-7Mo-xCo superaustenitic stainless steel, J. Mater. Sci. 57 (2022) 4771–4788.
[19] Q. Wang, L.J. Wang, Y.H. Sun, A.M. Zhao, W. Zhang, J.M. Li, H.B. Dong, K. Chou, The influence of Ce micro-alloying on the precipitation of intermetallic sigma phase during solidification of super-austenitic stainless steels, J. Alloy. Compd. 815 (2020) 152418.
[20] S.C. Zhang, J.T. Yu, H.B. Li, Z.H. Jiang, Y.F. Geng, H. Feng, B.B. Zhang, H.C. Zhu, Refinement mechanism of cerium addition on solidification structure and sigma phase of super austenitic stainless steel S32654, J. Mater. Sci. Technol. 102 (2022) 105–114.
[21] M. Sharma, I. Ortlepp, W. Bleck, Boron in heat-treatable steels: a review, Steel Res. Int. 90 (2019) 1900133.
[22] B. Hu, G. Trotter, Z. Wang, S. Chen, Z. Cai, I. Baker, Effect of boron and carbon addition on microstructure and mechanical properties of the aged gamma-prime strengthened alumina-forming austenitic alloys, Intermetallics 90 (2017) 36–49.
[23] Y.X. Zheng, F.M. Wang, C.R. Li, Y.L. Li, J. Cheng, Microstructural evolution, coarsening behavior of precipitates and mechanical properties of boron bearing steel 25Cr-MoNbB during tempering, Mater. Sci. Eng. A 712 (2018) 453–465.
[24] X.X. Yao, On the grain boundary hardening in a B-bearing 304 austenitic stainless steel, Mater. Sci. Eng. A 271 (1999) 353–359.
[25] L. Karlsson, Non-equilibrium grain boundary segregation of boron in austenitic stainless steel-III. Computer simulations, Acta Metall. 36 (1988) 25–34.
[26] L. Karlsson, H. Norden, Non-equilibrium grain boundary segregation of boron in austenitic stainless steel—IV. Precipitation behaviour and distribution of elements at grain boundaries, Acta Metall 36 (1988) 35–48.
[27] E.H. Jeong, S.G. Park, S.H. Kim, Y.D. Kim, Evaluation of the effect of B and N on the microstructure of 9Cr–2W steel during an aging treatment for SFR fuel cladding tubes, J. Nucl. Mater. 467 (2015) 527–533.
[28] K. Yang, Y. Ling, W. Yan, Y.Y. Shan, Preferential distribution of boron and its effect on microstructure and mechanical properties of (9-12)% Cr martensitic heat resistant steels, Acta Metall. Sin. 56 (2019) 53–65.
[29] J. Wang, Y.S. Cui, J.G. Bai, N. Dong, Y. Liu, C.L. Zhang, P.D. Han, The mechanism on the B addition to regulate phase precipitation and improve intergranular corrosion resistance in UNS S31254 superaustenitic stainless steels, J. Electrochem. Soc. 166 (2019) C600.
[30] J.G. Bai, Y.S. Cui, J. Wang, N. Dong, M.S. Qurashi, H.R. Wei, Y.C. Yang, P.D. Han, Effect of compression deformation on precipitation phase behavior of B-containing S31254 super austenitic stainless steel, J. Iron Steel Res. Int. 26 (2019) 712–719.
[31] L.H. Liao, J.Y. Li, Z.X. Zhao, F.H. Xu, W. Zhang, Precipitation and phase transformation behavior during high-temperature aging of a cobalt modified Fe-24Cr-(22-x)Ni-7Mo-xCo superaustenitic stainless steel, J. Mater. Sci. 57 (2022) 4771–4788.
[32] Y. Zhang, J.Y. Ma, H.B. Li, H. Wang, Y. Du, Z. Jiang, P.D. Han, Improved corrosion resistance of super austenite stainless steel by B-induced nucleation of Laves phase, Corros. Sci. 213 (2023) 110974.
[33] J.T. Yu, S.C. Zhang, H.B. Li, Z.H. Jiang, H. Feng, P. Xu, P.D. Han, Influence mechanism of boron segregation on the microstructure evolution and hot ductility of super austenitic stainless steel S32654, J. Mater. Sci. Technol. 112 (2022) 184–194.
[34] G.M. Carinci, Grain boundary segregation of boron in an austenitic stainless steel, Appl. Surf. Sci. 76 (1994) 266–271.
[35] W. Chen, M.C. Chaturvedi, N.L. Richards, G. McMahon, Grain boundary segregation of boron in INCONEL 718, Metall. Mater. Trans. A 29 (1998) 1947–1954.
[36] G. Da Rosa, P. Maugis, A. Portavoce, J. Drillet, N. Valle, E. Lentzen, K. Hoummada, Grain-boundary segregation of boron in high-strength steel studied by nano-SIMS and atom probe tomography, Acta Mater. 182 (2020) 226–234.
[37] J.M. Gao, J.Y. Ma, S. Yang, Z.S. Guo, J. Ma, H.B. Li, Z.H. Jiang, P.D. Han, Grain boundary co-segregation of B and Ce hindering the precipitates of S31254 super austenitic stainless steel, J. Mater. Res. Technol. 24 (2023) 2653–2667.
[38] M. Svoboda, A. Kroupa, J. Sopoušek, J. Vřešťál, P. Miodownik, Phase changes in superaustenitic steels after long-term annealing, Int. J. Mater. Res. 95 (2004) 1025–1030.
[39] P.Z. Cheng, N. Zhong, N.W. Dai, X.A. Wu, J. Li, Y.M. Jiang, Intergranular corrosion behavior and mechanism of the stabilized ultra-pure 430LX ferritic stainless steel, J. Mater. Sci. Technol. 35 (2019) 1787–1796.
[40] S.A. Hu, Y.Z. Mao, X.B. Liu, E.-H. Han, H. Hänninen, Intergranular corrosion behavior of low-chromium ferritic stainless steel without Cr-carbide precipitation after aging, Corros. Sci. 166 (2020) 108420.
[41] S. Hu, E.-H. Han, X. Liu, Atomic-scale evidence for the intergranular corrosion mechanism induced by co-segregation of low-chromium ferritic stainless steel, Corros. Sci. 189 (2021) 109588.
[42] R.K. Wang, Z.J. Zheng, Q.W. Zhou, Y. Gao, Effect of surface nanocrystallization on the sensitization and desensitization behavior of Super304H stainless steel, Corros. Sci. 111 (2016) 728–741.
[43] J. Qian, C.F. Chen, H.B. Yu, F. Liu, H. Yang, Z.H. Zhang, The influence and the mechanism of the precipitate/austenite interfacial C-enrichment on the intergranular corrosion sensitivity in 310 S stainless steel, Corros. Sci. 111 (2016) 352–361.
[44] M. Balakrishnan, G. Anburaj, S.S. Mohamed Nazirudeen, L. Neelakantan, R. Narayanan, Influence of intermetallic precipitates on pitting corrosion of high Mo superaustenitic stainless steel, Trans. Indian Inst. Met. 68 (2015) 267–279.
[45] M. Terada, D.M. Escriba, I. Costa, E. Materna-Morris, A.F. Padilha, Investigation on the intergranular corrosion resistance of the AISI 316L(N) stainless steel after long time creep testing at 600 °C, Mater. Charact. 59 (2008) 663–668.
[46] J.X. Wang, W. Shi, S. Xiang, R.G. Ballinger, Study of the corrosion behaviour of sensitized 904L austenitic stainless steel in Cl^- solution, Corros. Sci. 181 (2021) 109234.
[47] Z. Asghary, S. Abbasi, M. Seifollahi, M. Morakabati, Boron effect on phase transformation of σ and $M_{23}C_6$ in nimonic 105 superalloy, Mater. Res. Express 6 (2019) 116529.
[48] Z.F. Guo, H. Liang, M.J. Zhao, L.J. Rong, Effect of boron addition on hydrogen embrittlement sensitivity in Fe–Ni based alloys, Mater. Sci. Eng. A 527 (2010) 6620–6625.
[49] J.G. Li, C.L. Zhang, L. Xu, Z.X. Zhang, N. Dong, Y. Liu, J. Wang, Y.L. Zhang, L.X. Ling, P.D. Han, Effects of B on the segregation of Mo at the Fe-Cr-NiΣ5 (210) grain boundary, Physica B 568 (2019) 25–30.